



HAL
open science

Size dependent properties of Gd³⁺-free versus Gd³⁺-doped carbon dots for bioimaging application

Nazym Zhylkybayeva, Konstantin Paliienko, Anna Topchylo, Alexander Zaderko, Alain G elo en, Tatiana Borisova, Liudmyla Grishchenko, Ruslan Mariychuk, Valeriy Skryshevsky, Gauhar Mussabek, et al.

► To cite this version:

Nazym Zhylkybayeva, Konstantin Paliienko, Anna Topchylo, Alexander Zaderko, Alain G elo en, et al.. Size dependent properties of Gd³⁺-free versus Gd³⁺-doped carbon dots for bioimaging application. Scientific Reports, 2024, 14 (1), pp.27812. 10.1038/s41598-024-76500-z . hal-04781709

HAL Id: hal-04781709

<https://hal.science/hal-04781709v1>

Submitted on 13 Nov 2024

HAL is a multi-disciplinary open access archive for the deposit and dissemination of scientific research documents, whether they are published or not. The documents may come from teaching and research institutions in France or abroad, or from public or private research centers.

L'archive ouverte pluridisciplinaire **HAL**, est destin ee au d ep ot et  a la diffusion de documents scientifiques de niveau recherche, publi es ou non,  emanant des  tablissements d'enseignement et de recherche fran ais ou  trangers, des laboratoires publics ou priv es.



OPEN Size dependent properties of Gd³⁺-free versus Gd³⁺-doped carbon dots for bioimaging application

Nazym Zhylkybayeva^{1,2}, Konstantin Paliienko^{3,4}, Anna Topchylo^{5,6}, Alexander Zaderko⁶, Alain Gélöën⁷, Tatiana Borisova^{3,4}, Liudmyla Grishchenko⁵, Ruslan Mariychuk⁸, Valeriy Skryshevsky^{4,5}✉, Gauhar Mussabek^{1,2} & Vladimir Lysenko⁶

Gd³⁺-free carbon dots (CDs) were synthesized by one-step solvothermal method using urea, citric acid and 3-(trifluoromethyl)aniline as precursors. Additionally, Gd³⁺-doped CDs were prepared by incorporating gadolinium chloride (Gd³⁺ ions) into the synthesis. Size selection of the purified CDs was achieved through filter membranes ranging from 3 kDa to 100 kDa. The chemical composition and optical properties of the obtained samples were characterized by Energy dispersive X-ray (EDX), Fourier-transform infrared spectroscopy (FTIR), Dynamic Light Scattering (DLS), proton relaxation time measurements, Ultraviolet-visible (UV-vis) and fluorescence spectroscopies. A comparative analysis revealed a strong size-dependent behavior in the optical properties of both Gd³⁺-doped and Gd³⁺-free CDs. Furthermore, *in vitro* tests confirmed the non-cytotoxicity of Gd³⁺-doped CDs, indicating their potential applicability in biomedicine for magnetic resonance imaging (MRI) and red fluorescence-based cell and tissue imaging.

Keywords Carbon dots, Gd³⁺-doping, Fluorescence, Proton relaxation time, Cell toxicity, Fluorescent cell labelling

Due to their promising physicochemical properties, such as strong photoluminescence, biocompatibility, low toxicity, environmental friendliness, and low-cost fabrication, carbon dots (CDs) have emerged as one of the most fascinating materials for imaging-guided biomedical applications^{1–4}. The most developed bio-imaging techniques where CDs can be used as contrast agents are photoacoustic imaging (PAI)^{5,6}, fluorescence imaging (FLI)⁷, and magnetic resonance imaging (MRI)^{8–12}. Notably, MRI garners particular interest among these visualization techniques for its capability to produce detailed anatomical 3D representations of studied biological objects, leveraging various MRI contrast agents like heteroatom-doped CDs. For such applications, Gd³⁺, Fe²⁺, Mn²⁺, and Ni²⁺ are recognized as the predominant doping agents due to their ability to alter the physicochemical characteristics of the particles they dope and to reduce proton relaxation times. The incorporation of the metal ions into CDs induces profound alterations in their electron distribution and energy band gap, thus enabling the fine-tuning of the CDs' optical, electrical, chemical, and magnetic properties¹³. One of the primary methods for achieving such adjustment involves manipulation of the CDs' size.

Gd³⁺ ions are considered as optimal candidates for doping due to their distinctive paramagnetic properties¹⁴. However, it is widely recognized that free Gd³⁺ ions can be highly toxic (13–15 μM) because they inhibit calcium channels and cause neurologic and cardiovascular toxicity¹⁵. Minimizing the presence of free Gd³⁺ in Gd³⁺-doped CDs while preserving their superior magnetic resonance (MR) and fluorescence capabilities, would significantly enhance their applicability in bio-imaging contexts.

Numerous studies^{16–20} involving living cells and mice have been conducted to validate the low toxicity and high biocompatibility of Gd-doped CDs. These investigations revealed that Gd³⁺-doped CDs do not exhibit the pronounced toxicity associated with free Gd³⁺ ions, as the ions are complexed with the carboxyl groups within

¹Faculty of Physics and Technology, Al-Farabi Kazakh National University, 71, al-Farabi Ave., Almaty 050040, Kazakhstan. ²Institute of Information and Computational Technologies, 125 Pushkin Str., Almaty 050000, Kazakhstan. ³Palladin Institute of Biochemistry National Academy of Sciences of Ukraine, 9 Leontovicha Street, Kyiv 01054, Ukraine. ⁴Corporation Science Park, Taras Shevchenko University of Kyiv, 60 Volodymyrska Str., Kyiv 01033, Ukraine. ⁵Taras Shevchenko National University of Kyiv, 64/13 Volodymyrska Str., Kyiv 01601, Ukraine. ⁶Light Matter Institute, UMR-5306, Claude Bernard University of Lyon/CNRS, Université de Lyon, 69622 Villeurbanne Cedex, France. ⁷University of Lyon, UMR Ecologie Microbienne Lyon (LEM), CNRS 5557, INRAE 1418, Université Claude Bernard Lyon 1, VetAgro Sup, 69622 Villeurbanne, France. ⁸University of Presov, 17th November str. 1, Presov 08001, Slovakia. ✉email: skryshevsky@knu.uu

the CDs, mitigating their harmful effects. Additionally, these CDs demonstrate excellent water dispersibility and size uniformity. All these features make them excellent candidates for biomedical applications.

The quantum size effect in CDs has been the focus of numerous studies^{21–24}. This phenomenon becomes particularly influential at the nanoscale (< 10 nm), markedly affecting the CDs' electrical, optical, and magnetic properties. Several theoretical calculations were conducted to elucidate and verify the correlation between the size of CDs and their optical characteristics. These analyses confirmed that the energy difference between the highest occupied molecular orbital (HOMO) and the lowest unoccupied molecular orbital (LUMO) varies with the size of the CDs: while the size of the dots increases, the gap gradually decreases. And it was deduced that the strong emission of CDs comes from the quantum-sized carbon-material structure. Consequently, it was inferred that the intense luminescence exhibited by CDs is attributed to their quantum-sized carbon-based structural composition²⁵.

For example, Kaur and Bharij²⁶ synthesized CDs via plasma fusion and found that photoluminescence (PL) emission intensity peaks are influenced by the size of the CDs due to the quantum confinement effect. Similarly, Liu et al.²³ prepared graphene quantum dots (GQD) of various sizes through a simple and eco-friendly hydrothermal method. Their findings indicated that an increase in GQD size leads to a narrower energy gap, enhancing the likelihood of photon transitions and resulting in a redshift of the PL emission peak. Li et al.²⁷ observed distinct PL behaviors based on the size of the CDs: small CDs (1.2 nm) emit UV radiation (approximately 350 nm), medium-sized CDs (1.5–3 nm) generate visible light emission (400–700 nm) and larger CDs (3.8 nm) produce near-infrared emission (about 800 nm). They speculated that the intense emission from CDs is primarily due to the quantum-scale structure of graphite rather than the carbon-oxygen surface features. Additionally, Zhi et al.²⁸ obtained malic acid carbon dots (MACD) fractions and showed that their PL peaks shift from blue to cyan, yellowish and red. These shifts in PL emission are attributed to the narrowing of the band gap energy as the particle size increases. Wang et al.²⁹ synthesized amino-functionalized graphene quantum dots (AF-GQDs) with different sizes and observed that their absorption spectra exhibited a subtle blue shift with an increase in the size of the AF-GQDs. This phenomenon was linked to reduced conjugation due to a decrease in the molecular plane of the GQDs. Zhu et al.³⁰ produced three types of GQDs with sizes of 1–4 nm, 4–8 nm, and 7–11 nm by varying the reaction temperature, and these GQDs emitted PL in the range from blue and green to yellow. To investigate the correlation between particle size and PL emission, they conducted theoretical calculations and demonstrated that the particle size is related to the HOMO-LUMO gaps; as the size increases, the gap decreases progressively. Xin et al.³¹ prepared four types of CDs with different sizes using a one-step electrochemical oxidation method and discovered a link between the size of the CDs and their antibacterial properties. This relationship was explained by the synergy between the bacterial absorption capacity of CDs and the reactive oxygen species stimulated by the CDs.

Despite the significant amount of accumulated scientific data on studying the physicochemical properties of CDs, no research has been conducted specifically to clarify how the optical properties of CDs depend on the sizes of nanoparticles with and without Gd³⁺. In this work, we synthesized Gd³⁺-free and Gd³⁺-doped CDs by means of the solvothermal method and performed post-synthesis size selection of the CDs. We aimed to examine the size-dependent optical properties of both Gd³⁺-free and Gd³⁺-doped CDs, emphasizing the size-effect of these nanoparticles. Furthermore, we assessed the effects of these CDs on the proliferation of living cells in vitro. Notably, in vitro experiments indicated that Gd³⁺-doped CDs did not exhibit toxicity towards living cells, underscoring their potential for safe biomedical applications.

Results and discussion

Structure and chemical composition of CDs

Transmission Electron Microscopy (TEM) is one of the key methods for determining the structural features of fine nanoparticles, as in our case. However, it may not always be an informative tool when working with amorphous nanoparticles, which primarily consist of small molecular compounds. We attempted to capture TEM images of our particles, but due to their amorphous and small nature, we were unable to achieve good contrast. Due to poor contrast and non-representative results in the TEM images (see Fig. S1 in SM), we performed Dynamic Light Scattering (DLS) analysis instead to determine size distribution of the particles. As illustrated in Fig. 1a and b, the particle size distribution graphs indicate that the mean diameters of both types of CDs range from approximately 2 to 50 nm as a function of the used filters.

Zeta potential measurements were carried out using dynamic light scattering on a Malvern Z-sizer NANO. Figure 1c illustrates the zeta potential values of Gd³⁺-free and Gd³⁺-doped CDs, showing their pH-sensitive behavior. As one can see, the colloidal solutions of both types of CDs exhibit pH-dependent zeta potentials. A continuous decrease in zeta potential is observed as the pH increases, with Gd³⁺-free and Gd³⁺-doped CDs changing their zeta potential to the opposite sign with acidification of the medium.

At pH values below 3.8, Gd³⁺-free CDs exhibited positive zeta potential values can be attributed to 3-(Trifluoromethyl)aniline, an aromatic amine, used in the synthesis. This compound enriches the CDs with nitrogen, giving Gd³⁺-free CDs a positive zeta potential in the acid region. For Gd³⁺-doped CDs, the positive zeta potential was observed at pH below 7.2. The difference in the isoelectric points between the two types of CDs is likely due to the impact of the Gd ions, which carries a 3+ charge and can effectively neutralize negative surface charges, embedding itself into the Gd-CDs surface.

The chemical composition of both Gd³⁺-free and Gd³⁺-doped CDs was determined through Energy Dispersive X-ray Spectroscopy (EDX) and Fourier Transform Infrared Spectroscopy (FTIR). Figure 2a clearly illustrates that both varieties of CDs predominantly consist of carbon and oxygen atoms, with significantly lesser amounts of fluorine and, where applicable, gadolinium. Notably, the Gd³⁺-free CDs, as expected, exhibit no traces of gadolinium, thereby confirming their classification as gadolinium-free.

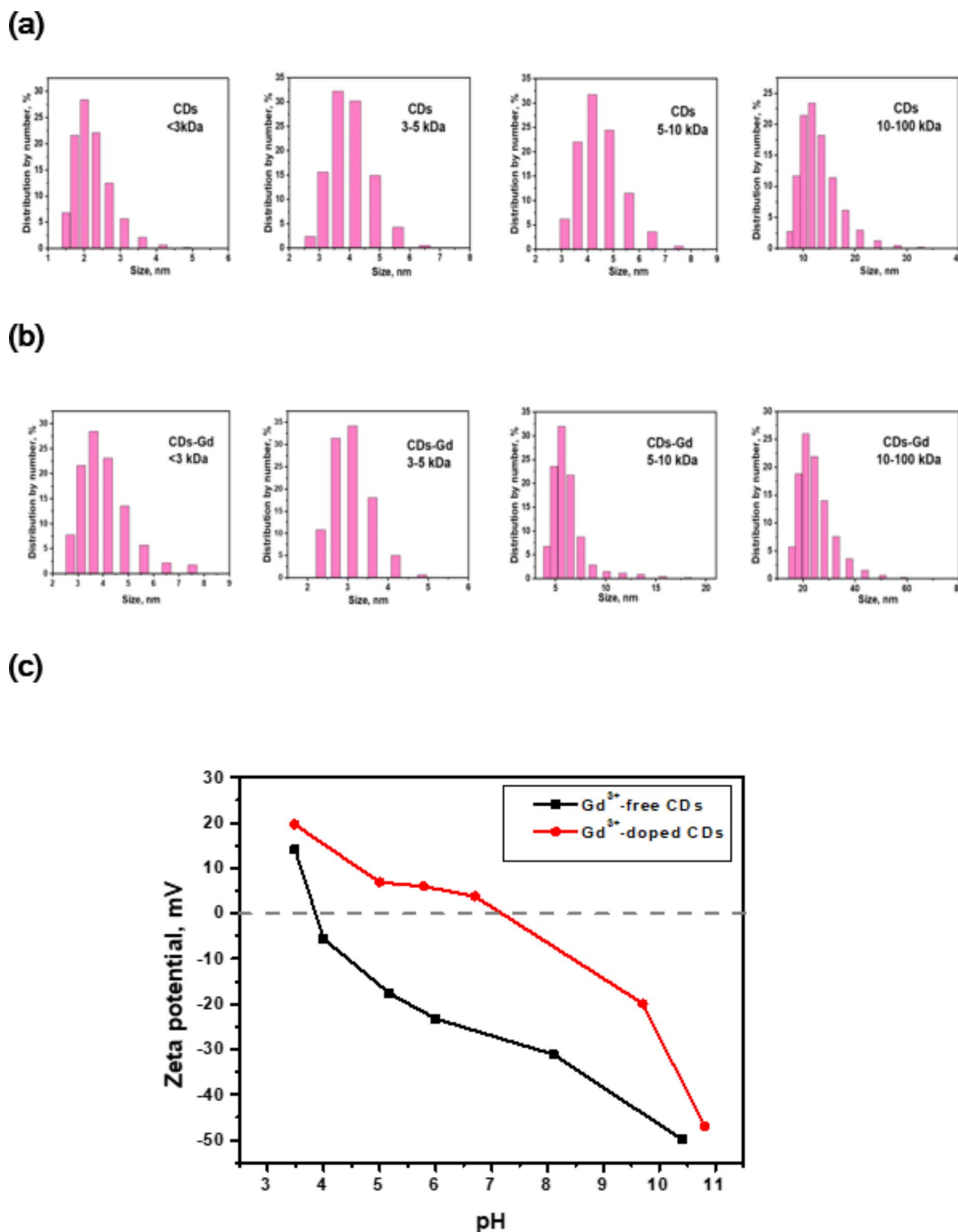


Fig. 1. Gd³⁺-free (a) and Gd³⁺-doped (b) CDs size distribution; (c) Zeta potential of Gd³⁺-free and Gd³⁺-doped CDs at different pH.

FTIR analysis was conducted to examine the molecular structure of both Gd³⁺-free and Gd³⁺-doped CDs, with the results presented in Fig. 2b. The spectra were recorded over the range of 600 to 4000 cm⁻¹.

The FTIR spectra revealed the presence of various functional groups that contribute to forming a protective layer on the CDs' surface. A broad band observed between 3400 and 3000 cm⁻¹ corresponds to stretching vibrations $\nu(\text{O-H})$ of hydrogen-bonded hydroxyls. The peaks in the range of 3000–2800 cm⁻¹ are attributed to the stretching vibrations $\nu(\text{C-H})$ ³². An intense band around 1600 cm⁻¹ likely results from bending vibrations

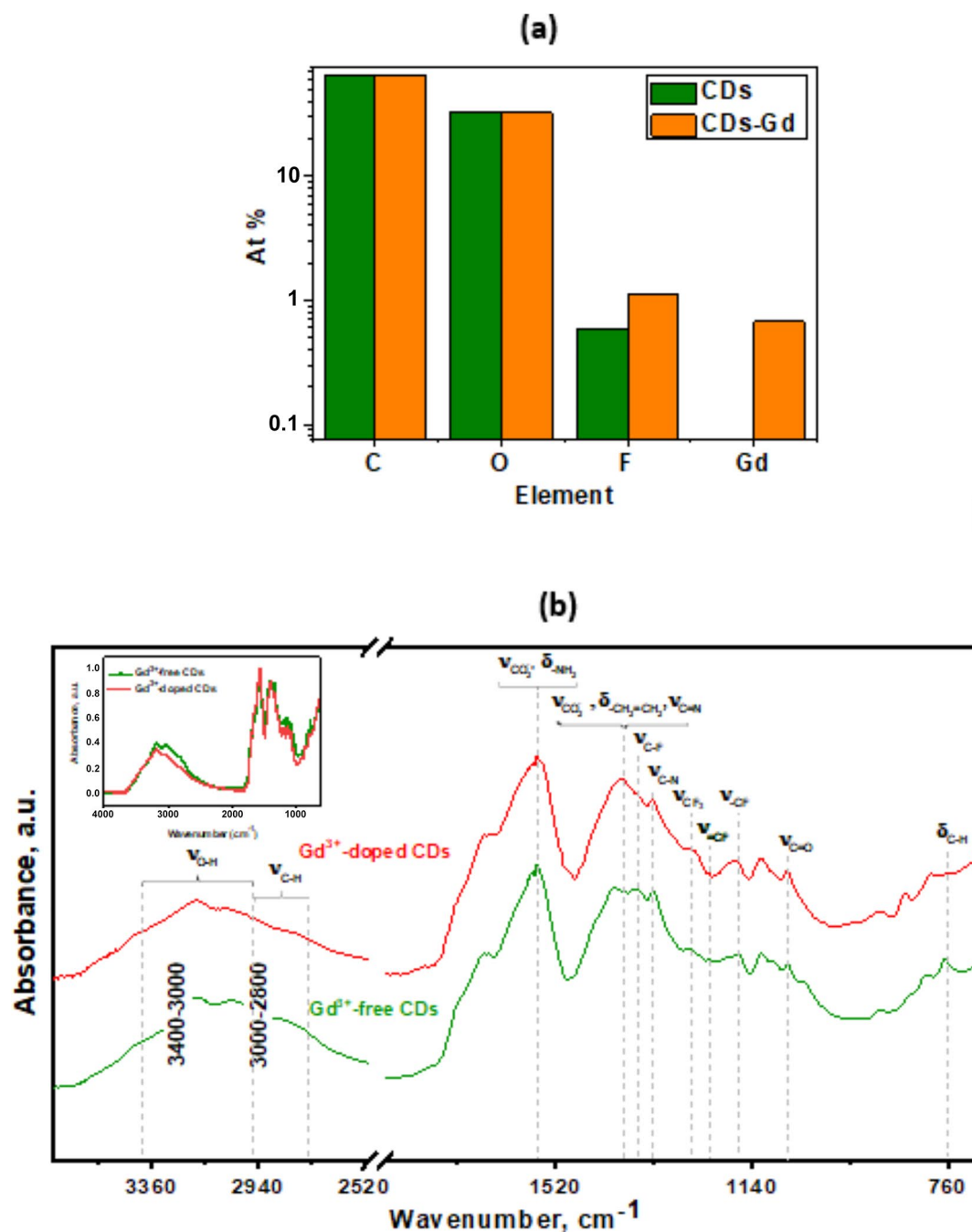


Fig. 2. (a) EDX analysis and (b) FTIR analysis of Gd³⁺-free and Gd³⁺-doped CDs.

(deformations) of free groups $\delta(-\text{NH}_2)$, water molecules or C=C bonds in benzene rings and other double bonds^{33,34}, along with asymmetric stretching vibrations of carboxylate groups $\nu_{\text{as}}(-\text{CO}_2^-)$ ³⁵. The band 1420 cm⁻¹ is associated with symmetric stretching vibrations of carboxylate groups $\nu_{\text{s}}(-\text{CO}_2^-)$, scissoring vibrations of the CH₂ fragment in vinyl groups $\delta_{\text{s}}(-\text{CH}_2=\text{CH}_2)$, and stretching vibrations $\nu(\text{C}=\text{N})$. A band at 1070 cm⁻¹ is attributed to $\nu(\text{C}-\text{O})$ stretching vibrations and may include a contribution from isopropanol³⁶.

Notably, a strong IR band with a maximum at 1166 cm⁻¹ is clearly observed, corresponding to the C-F bond³⁷. When the fluorine atom is connected through sp³-hybridization, the C-F bond is considered covalent, with stretching vibration absorption at peaks near 1221 cm⁻¹³⁸ and CF₃ bond at 1260 cm⁻¹³⁹. According to⁴⁰, an asymmetric C-F stretching vibration at 1330 cm⁻¹ appears with strong intensity.

The surface chemistry of both Gd³⁺-free and Gd³⁺-doped CDs appears very similar, suggesting that the presence of Gadolinium does not significantly affect the surface chemistry of the CDs.

Figure 3 shows the schematic representations of the molecular structures for both fluorinated Gd³⁺-free and Gd³⁺-doped CDs. In Fig. 3a, the 3D structure of Gd³⁺-free CDs is depicted, where carbon atoms are illustrated in gray, oxygen atoms – in red, hydrogen atoms – in white, fluorine atoms – in turquoise, and nitrogen atoms – in

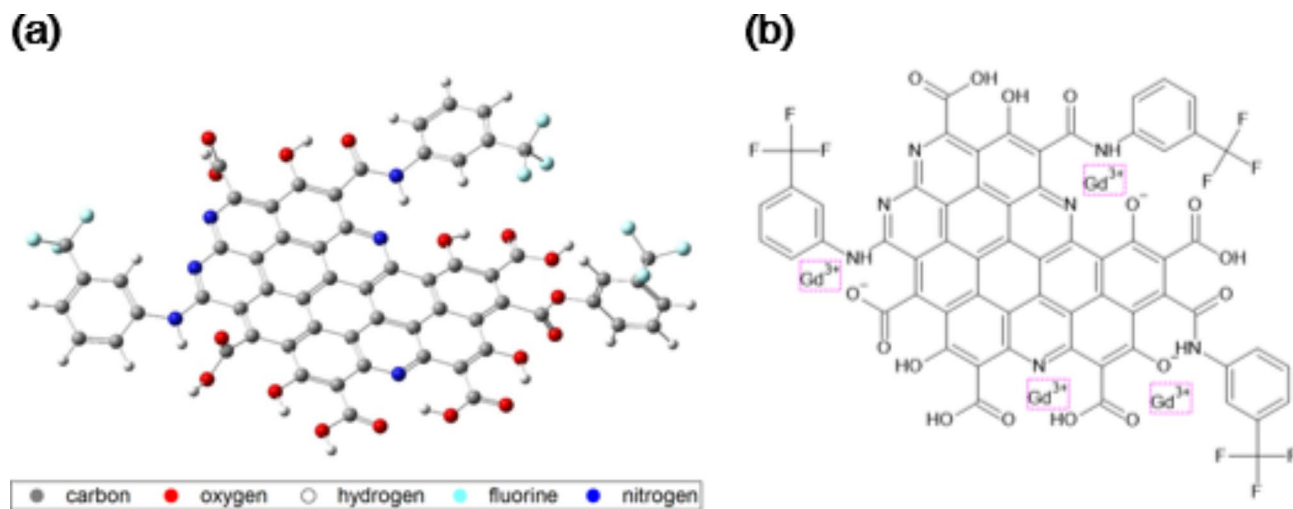


Fig. 3. Schematic structure of (a) Gd^{3+} -free (carbon atoms are in gray, oxygen – in red, hydrogen – in white, fluorine– in turquoise, and nitrogen atoms – in blue) and (b) Gd^{3+} -doped CDs.

blue. Figure 3b displays the 2D model of the Gd^{3+} -doped CDs, highlighting possible places for localization for the Gd^{3+} ions.

Proton relaxation times measurements

Figure 4a and b present the outcomes of longitudinal (T_1) and transverse (T_2) proton relaxation time measurements performed on Gd^{3+} -free and Gd^{3+} -doped CDs. The T_1 and T_2 values for pure water are added for comparison. A significant distinction in relaxation times is evident between Gd^{3+} -free and Gd^{3+} -doped CDs. One can see that for both types of CDs with sizes below 5 kDa, the T_1 and T_2 values closely approximate those of pure water (4150 ± 20 ms). However, for the CDs larger than 10 kDa, the difference in both longitudinal and transverse proton relaxation times becomes markedly pronounced. In particular, the T_1 and T_2 values for the Gd^{3+} -doped CDs are significantly reduced, nearly two orders of magnitude shorter than those observed for the Gd^{3+} -free CDs, underscoring the impact of Gd^{3+} ion incorporation. Indeed, the sensitivity of proton relaxation times to the presence of paramagnetic ions in solutions is a well-known phenomenon⁴¹. It is noteworthy to mention the preferential incorporation of Gd^{3+} ions into the larger carbon dots (CDs), ranging in size from 10 to 100 kDa. This selective incorporation significantly influences the magnetic properties of the CDs, particularly determining their application in magnetic resonance imaging (MRI) as contrast agents.

Optical properties

UV-VIS absorbance

Figure 5 illustrates the absorption spectra of the Gd^{3+} -free and Gd^{3+} -doped CDs, with Fig. 5a and b highlighting the spectra of small (< 3 kDa) and large (10–100 kDa) Gd^{3+} -free CDs, respectively. Conversely, Fig. 5c and d display the absorption spectra of Gd^{3+} -doped CDs.

According to the literature data⁴², high-energy absorption bands exceeding 4.5 eV are attributed to $\pi \rightarrow \pi^*$ transitions, specifically involving sp^2 hybridized aromatic carbons, indicative of $\text{C}=\text{C}$ aromatic bonds. The subsequent peaks observed in the range of 3.2 to 3.6 eV are correlated with the intrinsic absorption related to $n \rightarrow \pi^*$ transitions in the $\text{C}=\text{O}$, $\text{C}=\text{N}$ and $\text{C}-\text{F}$ bonds present in the carbon cores. Absorption bands falling below 3 eV stem from transitions associated with surface states of the particles. It is important to note that the $n \rightarrow \pi^*$ transitions and the broad absorption bands corresponding to surface states often exhibit overlapping features, rather than being distinctly separate. Hence, band 5 is also associated with photoinduced electronic transitions within surface chemical bonds. Regarding band 6, this feature may be ascribed to the integration of nitrogen into the sp^2 carbon lattice or to surface states involving nitrogen and/or fluorine, further illustrating the complex interactions and structural nuances within the carbon dots.

The comparison reveals that the small (< 3 kDa) Gd^{3+} -free and Gd^{3+} -doped CDs exhibit remarkably similar absorption spectra. The spectral features, following deconvolution of the experimental data, show identical intensities and spectral positions. However, a distinct difference emerges when examining the absorption spectra of the larger CDs (10–100 kDa). The intensity of peaks, revealed through deconvolution (with Figures S2–S8 in the Supplementary Material providing detailed deconvolution processes), demonstrates a noticeable disparity. Specifically, the Gd^{3+} -doped CDs exhibit higher absorption intensities than their Gd^{3+} -free counterparts. In particular, the spectral band between 4.5 and 6 eV is significantly more pronounced for the Gd^{3+} -doped CDs. Furthermore, the relative intensity of the spectral band centered around 3 eV, compared to that at 2 eV, is also elevated in the Gd^{3+} -doped CDs, highlighting the substantial impact of gadolinium doping on the optical properties of the CDs.

The observed spectral resemblance between the small (< 3 kDa) Gd^{3+} -free and Gd^{3+} -doped CDs can be attributed to their similar low-molecular chemical compositions, independent on the presence or absence of

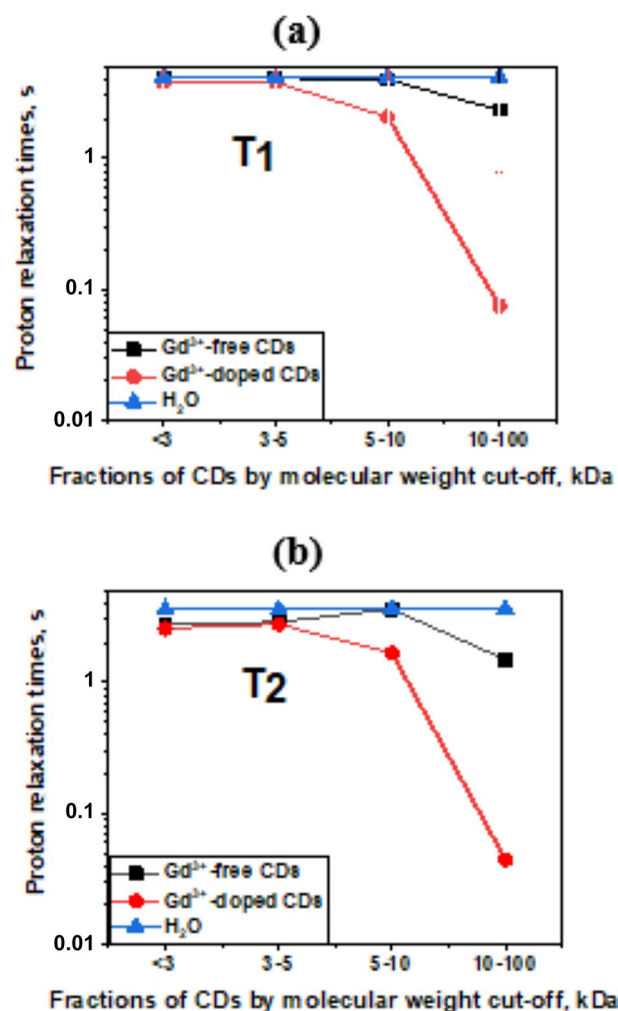


Fig. 4. (a) Longitudinal (T_1) proton relaxation times dependence on sizes of Gd^{3+} -free and Gd^{3+} -doped CDs; (b) Transverse (T_2) proton relaxation times dependence on sizes of Gd^{3+} -free and Gd^{3+} -doped CDs.

Gd^{3+} ions. This observation suggests that Gd^{3+} ions do not significantly interact with the smallest CDs. On the other hand, the noticeable spectral differences observed between the larger (10–100 kDa) Gd^{3+} -free and Gd^{3+} -doped CDs can be explained by the incorporation of Gd^{3+} ions into the latter. In particular, the enhanced UV-visible absorption intensity seen in the Gd^{3+} -doped CDs can be attributed to their heightened polarizability. This, in turn, leads to an increased optical absorption cross-section, a result of integrating the highly charged Gd^{3+} ions into the larger CDs' structure.

Fluorescence

Figure 6 displays fluorescence (FL) excitation/emission (FLE) maps of Gd^{3+} -free and Gd^{3+} -doped CDs recorded under UV and visible light excitation, respectively. Figure 6a presents FL/FLE maps for CDs of various sizes, excited in the 250–380 nm range, while Fig. 6b displays these maps for the Gd^{3+} -doped CDs. Across all the FL/FLE maps in Fig. 6, two distinct spectral regions are identified: one related to an excitation at 370 nm and the other at 270 nm. For smaller particles, the FL peak maximum aligns with an excitation at 370 nm, whereas for larger particles, the peak maximum corresponds to excitation at 270 nm. With increasing particle size, the absolute FL intensity excited at 370 nm (associated with smaller particles) diminishes, and the ratio of fluorescence intensities upon excitation at 270 nm to 370 nm (I_{270}/I_{370}) increases. Mirroring the absorption spectra for the smaller (<3 kDa) Gd^{3+} -free and Gd^{3+} -doped CDs, their FL/FLE spectral maps are virtually indistinguishable in terms of intensity and spectral characteristics. This similarity suggests that both types of CDs share an identical low-molecular-weight chemical composition, unaffected by the presence or absence of Gd^{3+} ions. In contrast, the FL intensities of the largest (10–100 kDa) Gd^{3+} -doped CDs are lower compared to the Gd^{3+} -free CDs within the same size range. Considering their higher absorption values, it can be inferred that the incorporation of Gd^{3+} ions enhances the likelihood of non-radiative recombination events, affecting the fluorescence properties of the CDs. FL/FLE spectral maps (at excitation range 250–380 nm) with absolute maximum values adapted for each map are given in the Supplementary (Figure S9).

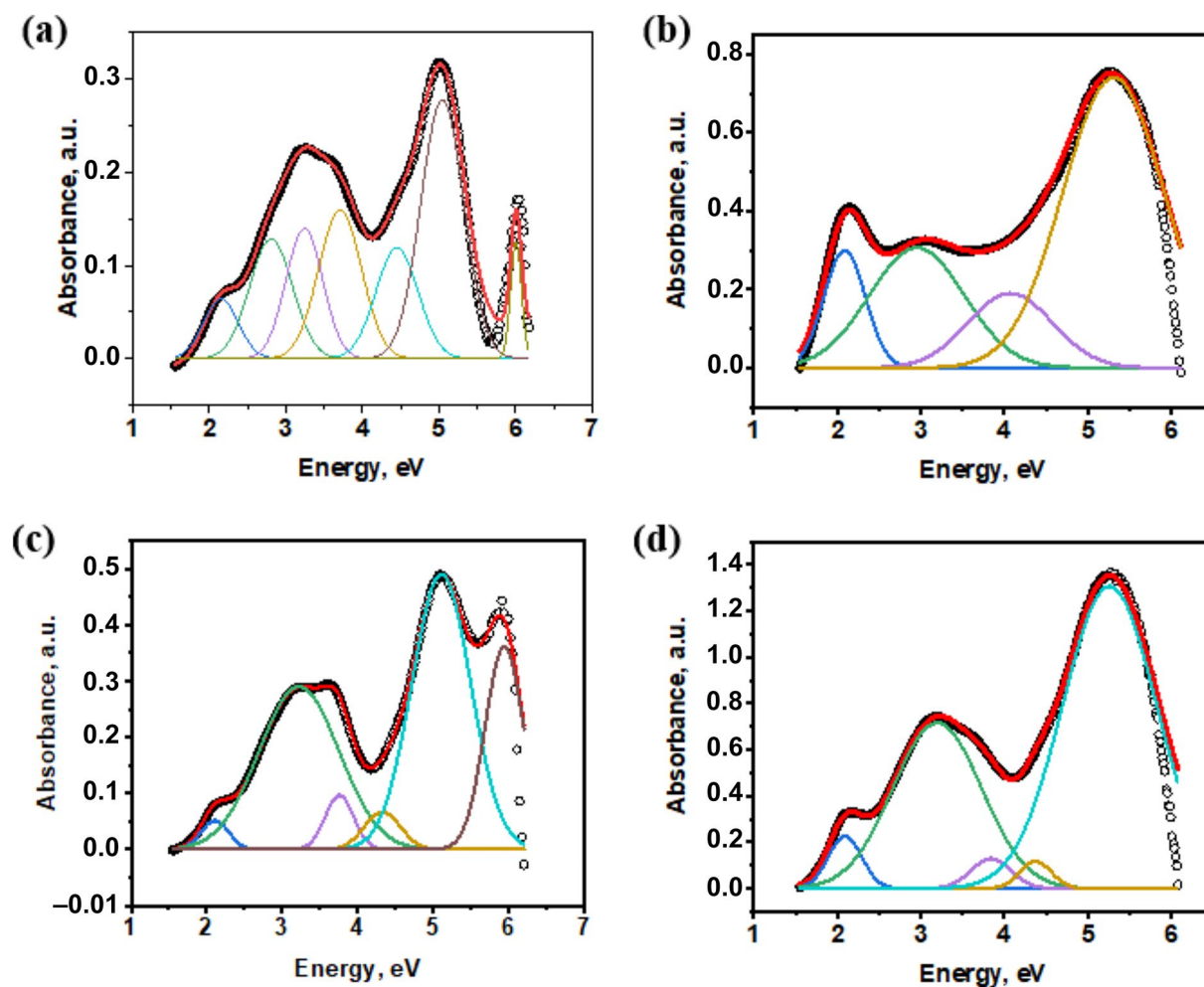


Fig. 5. UV-visible absorbance spectra of: (a) Gd^{3+} -free CDs with sizes < 3 kDa; (b) Gd^{3+} -free CDs with sizes 10–100 kDa; (c) Gd^{3+} -doped CDs with sizes < 3 kDa; (d) Gd^{3+} -doped CDs with sizes 10–100 kDa.

Figure 6c and d show, respectively, FL/FLE maps upon excitation of Gd^{3+} -free and Gd^{3+} -doped CDs of various sizes in the range of 400–560 nm. Across these maps (except for Gd^{3+} -free CDs with sizes 10–100 kDa) a prominent maximum FL intensity is observed, centered around 430 nm excitation. This FL peak, dominant in smaller particles (< 10 kDa), gradually diminishes as the size of the nanoparticles increases. This indicates that the FL/FLE spectral region, excited between 400 and 470 nm and emitting at < 600 nm, is characteristic of small, low-molecular-weight species. Conversely, the intensity of the red fluorescence in Gd^{3+} -free CDs, excited at 540 nm, intensifies and becomes maximal for larger particles (10–100 kDa). In comparison, the intensity of similar red fluorescence in Gd^{3+} -doped CDs is significantly reduced. This observation suggests that the incorporation of Gd^{3+} ions into larger CDs results in a pronounced quenching of their red fluorescence, highlighting the impact of Gd^{3+} ions on the fluorescence properties of the CDs, particularly in altering their emission profiles (see also Figure S10).

Cell toxicity

Figure 7 shows the evolution of cell indexes in the presence of increasing concentrations of Gd^{3+} -free CDs (a) or Gd^{3+} -doped CDs (b) during 24 h. The data indicate that Gd^{3+} -free CDs do not affect cell indexes, demonstrating complete biological compatibility at the tested concentrations (as shown in Figure S11 (a) in the Supplementary Materials). However, cell indexes slightly decreased when exposed to the highest concentration of Gd^{3+} -doped CDs (Figure S11 (b) in the Supplementary Materials), suggesting a certain degree of toxicity. The toxicity of these CDs can be qualitatively evaluated by analyzing the time dependent changes in slope values; a lower slope indicates higher cytotoxicity. Following the 24 exposures, the culture medium containing CDs was replaced with fresh medium without CDs, allowing for further assessment of any long-term effects or recovery. This had no effect on the cell indexes of cells exposed to CDs. The slopes of cell indexes for cells exposed to Gd^{3+} -doped CDs showed an increase after the washout, indicating the absence of any lasting detrimental effects from these CDs. The impact of Gd^{3+} -doped CDs on cell viability can be qualitatively assessed by the slope of cell index values, the lower the slope, the higher the impact. Indeed, the higher the concentration of Gd^{3+} -doped CDs, the more significant was the decrease in the slope of the cell index. The highest concentration of Gd^{3+} -doped CDs

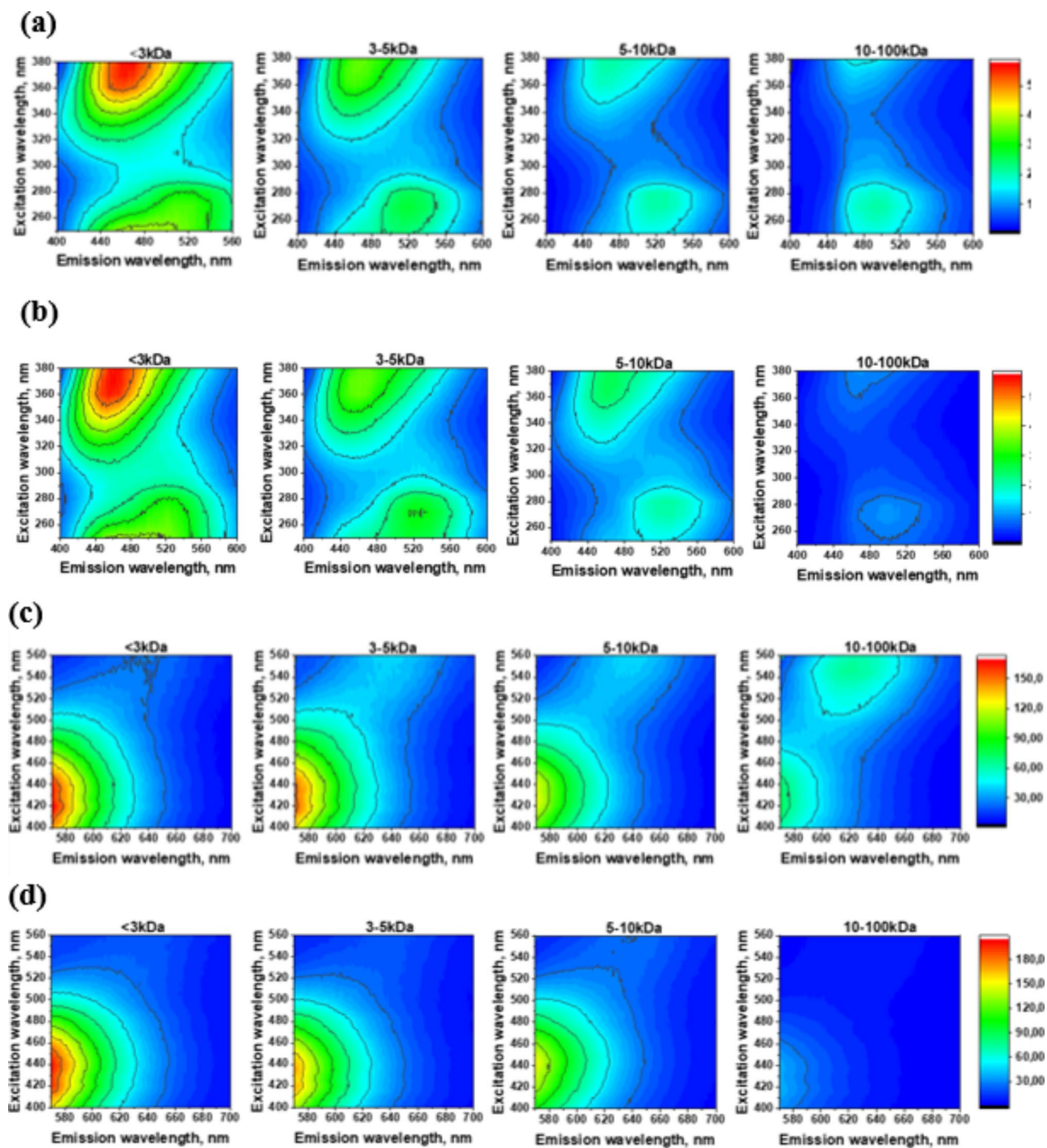


Fig. 6. FL excitation/emission maps in the UV-visible region: (a, c) Gd^{3+} - free CDs, (b, d) Gd^{3+} - doped CDs.

(10 $\mu\text{g}/\text{mL}$) resulted in a minor reduction in the slope of the cell index. At the lower concentrations (1–5 $\mu\text{g}/\text{mL}$), Gd^{3+} - doped CDs exhibited no significant effects, highlighting the sensitivity of the cell index measurement. This slight reduction in cell index, suggesting a minimal impact potentially limited to cell adhesion, is corroborated by microscopic observations (Fig. 9), which revealed no changes in cell shape and structure, thus suggesting the absence of toxicity.

Fluorescent cell labeling

In order to test the ability of Gd^{3+} - doped CDs to serve as bimodal contrast agent, human carcinoma A549 cells were loaded with them at various concentrations (5 and 10 $\mu\text{g}/\text{mL}$). Figure 8 demonstrates the uneven distribution of fluorescence intensity on photomicrographs. The enhanced visibility within the cells is attributed

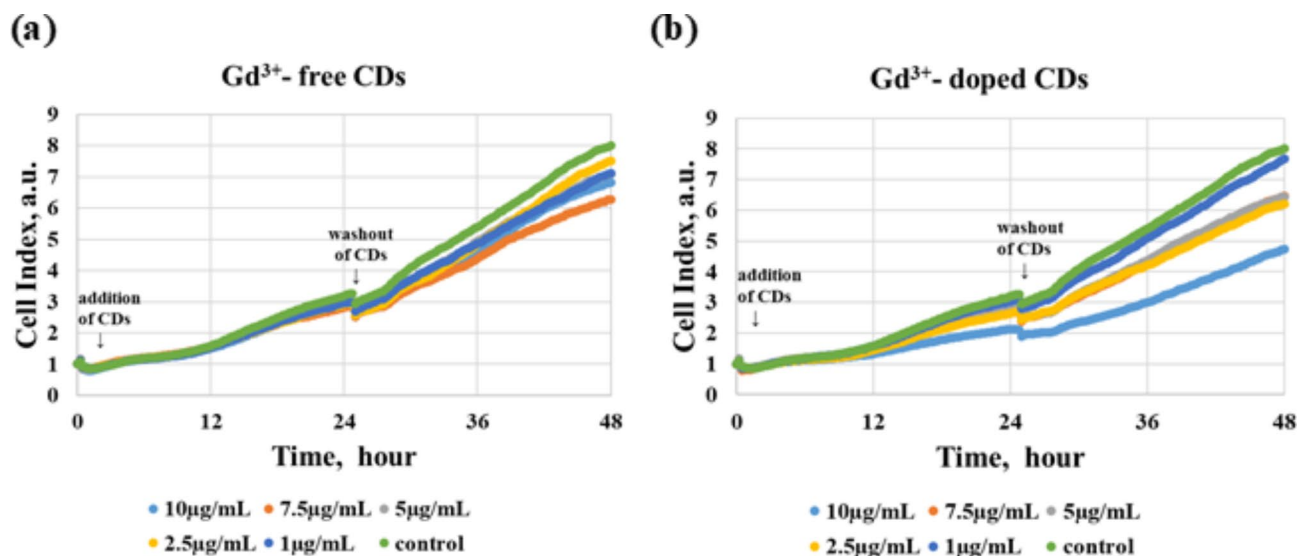


Fig. 7. Evolution of cell index of A549 cells exposed to increasing concentrations of (a) Gd^{3+} - free CDs and (b) Gd^{3+} - doped CDs during 24 h and after washout.

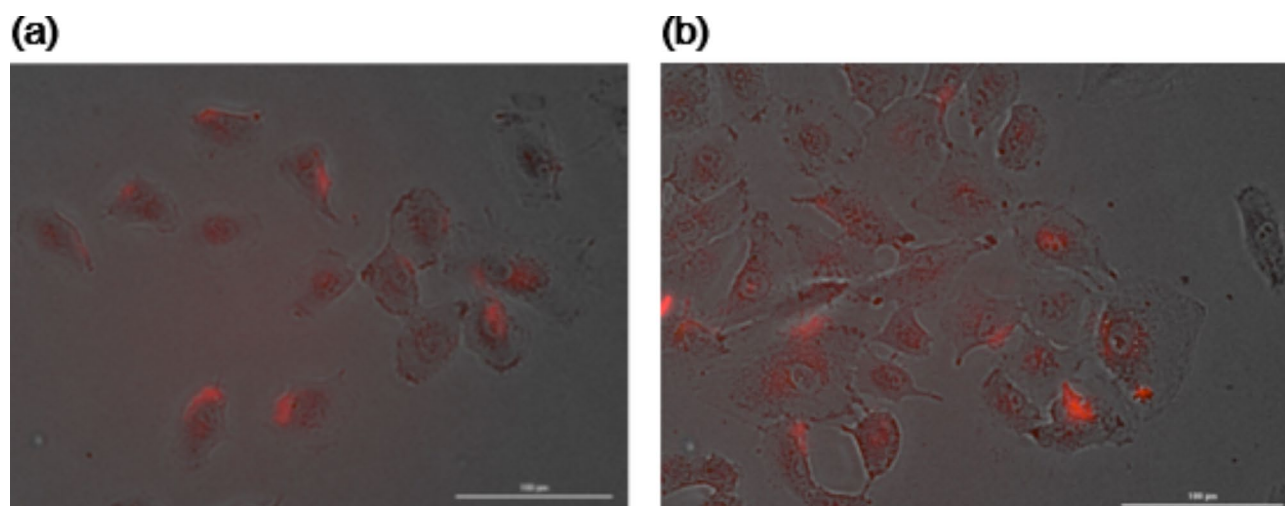


Fig. 8. Fluorescent microscopy images of human carcinoma A549 cells labeled with Gd^{3+} - doped CDs at different concentrations: (a) 5 $\mu\text{g}/\text{mL}$; (b) 10 $\mu\text{g}/\text{mL}$.

to the fluorescent properties of the Gd^{3+} - doped CDs. Notably, the most intense fluorescent spots are not located within the nucleus. While some nuclei appear slightly labeled, it's likely that the labeling is positioned outside the nuclei, with most nuclei remaining unlabeled. It should be noted that the incorporation of Gd^{3+} - doped CDs into cells didn't alter the cells' size and shape, indicating their biocompatibility. This evidence supports the potential of Gd^{3+} - doped CDs to serve as effective fluorescent markers in cellular imaging applications, as documented in references⁴³.

Conclusions

The Gd^{3+} free and Gd^{3+} -doped CDs were successfully synthesized through a straightforward one-step solvothermal method and categorized into four size-based fractions. Our findings reveal that Gd^{3+} ions preferentially incorporate into larger CDs (10–100 kDa) while exhibiting minimal interaction with the smaller ones (<3 kDa). The study indicates that the presence of Gd^{3+} ions in smaller CDs increases the probability of photo-induced non-radiative recombination events. Conversely, their integration into the larger CDs significantly diminishes red fluorescence, suggesting an alteration in their optical properties. In vitro experiments confirmed the global non-toxic nature of both Gd^{3+} - free and Gd^{3+} - doped CDs, highlighting their biocompatibility. The straightforward synthesis process, coupled with their low toxicity and the unique optical properties of the Gd^{3+} - doped CDs, underscores their potential for biomedical applications. Specifically, their efficacy as fluorescent cell

markers and low proton relaxation times offer promising opportunities for bi-modal bio-imaging (fluorescence and MRI) techniques, paving the way for advanced diagnostic and therapeutic applications.

Materials and methods

Synthesis of CDs

The synthesis of CDs was carried out according to the patented protocol⁴⁴. To synthesize CDs, 3 g (15.6 mmol) of anhydrous citric acid (Sigma-Aldrich, suitable for cell culture) and 6 g (0.10 mol) of urea (Sigma-Aldrich, ACS reagent) were dissolved and made up to the 30 mL volume with DMF solvent (Sigma-Aldrich, anhydrous, 99.8%). Subsequently, 0.425 g (2.65 mmol) of 3-(trifluoromethyl)aniline (Sigma-Aldrich, ≥ 99%) was added to the solution. The resultant mixture was then equally divided into two parts. To the second portion, 242.4 mg (0.65 mmol) of gadolinium(III) chloride hexahydrate (Sigma-Aldrich, 99%) was added and dissolved with the aid of a magnetic stirrer, ensuring the formation of a clear solution. Both solutions were subsequently transferred into sealed Pyrex glass ampoules. These ampoules were then placed in a PTFE-lined stainless-steel autoclave and placed in an oven at 180 °C for 8 h. Post-synthesis, the samples were categorized as Gd³⁺-doped carbon dots (CDs-Gd) for the gadolinium-containing sample, and Gd³⁺-free carbon dots (CDs) for the sample without gadolinium.

The purification of Gd³⁺-free and Gd³⁺-doped CDs consisted of three stages: preliminary purification, dialysis and fractionation.

Preliminary purification is obligatory for coarse particles elimination. The ampoules were opened; and their contents were diluted with water to 15 mL. The colloidal solutions were then transferred to ultra-filtration spin columns (centrifugal concentrators), specifically Vivaspin[®] 20 (100,000 molecular weight cut-off (MWCO), Polyethersulfone (PES) membrane), and centrifuged at 3000 g for 1 h. This process resulted in a fraction with a conditional molecular weight of less than 100 kDa.

Dialysis was performed to remove low molecular components. For this purpose, dialyzing sacks made of membrane with a nominal filter rating of 3'500 MWCO (ZelluTrans ROTH[®] Regenerated Cellulose Tubular Membrane, flat width 19 mm, wall thickness 25 µm, volume per length 1.15 mL/cm) were utilized. This step lasted for 190 h. Liquids that permeated through the membrane pores of 100'000 MWCO were collected and transferred into dialyzing sacks 20 cm in length featuring membrane pores of 3'000 MWCO. Dialyzing sacks were filled with 15 mL of colloid solutions containing synthesized Gd³⁺-free and Gd³⁺-doped CDs and placed separately into 5000 mL vessels with deionized water. The water in these vessels was replaced three times daily over an 8-day dialysis period. Following this process, the initial fraction, labeled as "100 – 10 kDa", was collected. The concentrations of solutions containing Gd³⁺-free and Gd³⁺-doped CDs were determined using a gravimetric technique, with values of 270 µg/mL and 130 µg/mL respectively.

The fractionation procedure was implemented to segregate the synthesized particles into distinct size-based fractions, allowing for the detailed investigation of their properties within separate groups. Table 1 outlines the steps involved in the fractionation process.

Therefore, 4 fractions of Gd³⁺- free CDs and Gd³⁺- doped CDs were obtained: lower than 3 kDa, 3–5 kDa, 5–10 kDa and 10–100 kDa.

Optical characterization

After purification, UV-visible absorption and fluorescence spectra were measured. The UV-visible absorption spectra were acquired using a Shimadzu UV-2700 spectrophotometer (Shimadzu, Japan). Meanwhile, fluorescence excitation/emission maps were recorded on a Cary Eclipse Fluorescence Spectrophotometer (Agilent Technologies, USA) with a xenon flash lamp (80 Hz) as the excitation source.

Proton relaxation measurements

Proton relaxation times T₁ and T₂ were studied by means of Bruker 60 MHz equipment MQ60 (ND 2605, Bruker Optic GmbH, Rheinstetten, Germany). Data was analyzed using the "Bruker theminispac" application. We analyzed 300 µL of colloidal solution of the nanoparticles in the vials for all experiments.

Cell toxicity studies

Cell number measurements were conducted using a non-destructive impedance-based technique called xCELLigence (ACEA Biosciences Inc., Biotek, Colmar, France). The cells were cultured on a specialized plate with electrodes on the bottom. The system measures electrical impedance across interdigitated microelectrodes located at the bottom of the culture wells. The measurements involved applying an alternative excitation signal (with a control voltage amplitude of 20 mV) at 3 different frequencies (10, 25, and 50 kHz) through the microelectrodes in the E-plates while monitoring the voltage drop across the electrodes. The impedance data was processed over time, resulting in a cell index value. The cell index was directly related to factors

Step	Process	Samples
1	Centrifugate content of sacks after dialysis in Vivaspin20 10'000 MWCO, RCF: 4'000 g, Time: 3 h	Supernatant: 10–100 kDa, Filtrate: 3.5–10 kDa
2	Centrifugate the filtrate 3.5–10 kDa in Vivaspin20 5'000 MWCO, RCF: 4'000 g, Time: 2 h	Supernatant: 5–10 kDa, Filtrate: lower 5 kDa
3	Centrifugate the filtrate lower 5 kDa in Vivaspin20 5'000 MWCO, RCF: 3'000 g, Time: 2 h	Supernatant: 3–5 kDa, Filtrate: lower 3 kDa

Table 1. Fractionation procedure of Gd³⁺- free CDs and Gd³⁺- doped CDs.

such as cell number, cell surface area, and adhesion. Among these factors, cell number was found to be the primary determinant of the cell index value for a given cell line. The impedance measurement method used was non-destructive and allowed real-time continuous monitoring of cell proliferation under various conditions, including the presence of CDs and after their removal (washout), on the same cell population. To compare the effects of increasing concentrations of Gd³⁺- free and Gd³⁺- doped CDs on cell proliferation, the cell index slopes on normalized curves were measured. Each curve presented the average cell index measured in four wells. Experiments were carried out on adenocarcinomic human alveolar basal epithelial A549 cells. Cells have been seeded at 2500 /well, and allowed to grow for 48 h, until reaching a cell index value close to 1. Then culture medium has been replaced with the same composition plus increasing concentrations of NPs. Cells have been kept for 24 h then the culture medium has been replaced with fresh culture medium without NPs (washout).

Fluorescence cell labelling

Images were taken at magnification from magnification x20 using a Cytation 3 cell imaging reader (Biotek Instrument Inc., Colmar, France) on cells fixed with formalin 10% (Sigma Aldrich). Fluorescence was measured with the filter Ex586/Em 647 (Berger et al. 2015)⁴⁵.

The data are presented as mean values \pm SEM. Statistical analysis was performed with StatView 4.5 software (Abacus Corporation, Baltimore, MD, USA) for Windows. Data were analyzed using a one-way ANOVA followed by a Fisher's protected least significance difference (PLSD) post hoc test. The significance level was accepted at $p < 0.05$.

Data availability

The datasets used and analyzed during the current study are available from the corresponding author upon reasonable request.

Received: 14 August 2024; Accepted: 14 October 2024

Published online: 13 November 2024

References

- Li, H. et al. Recent advances in carbon dots for bioimaging applications. *Nanoscale Horiz.* **5**, 218–234. <https://doi.org/10.1039/C9NH00476A> (2020).
- Boakye-Yiadom, K. O. et al. Carbon dots: Applications in bioimaging and theranostics. *Int. J. Pharm.* **564**, 308–317. <https://doi.org/10.1016/j.ijpharm.2019.04.055> (2019).
- Zhu, P. et al. Carbon Dots in Biomedicine: A Review. *ACS Appl. Bio Mater.* **5**, 2031–2045. <https://doi.org/10.1021/acsabm.1c01215> (2022).
- Paliienko, K. et al. Green synthesis of biocompatible Gd³⁺-doped ultrasmall carbon-based nanohybrids from coffee wastes. *Carbon Resour. Convers.* **7**, 100197. <https://doi.org/10.1016/j.crcon.2023.09.001> (2024).
- Dubyk, K. et al. Bio-distribution of carbon nanoparticles studied by photoacoustic measurements. *Nanoscale Res. Lett.* **17**, 127. <https://doi.org/10.1186/s11671-022-03768-3> (2022).
- Isaiev, M. et al. Application of the photoacoustic approach in the characterization of nanostructured materials. *Nanomaterials* **12**, 708. <https://doi.org/10.3390/nano12040708> (2022).
- Li, C. et al. Advanced fluorescence imaging technology in the near-infrared-II window for biomedical applications. *J. Am. Chem. Soc.* **142**, 14789–14804. <https://doi.org/10.1021/jacs.0c07022> (2020).
- Lundervold, A. S. & Lundervold, A. An overview of deep learning in medical imaging focusing on MRI. *Z. Med. Phys.* **29**, 102–127. <https://doi.org/10.1016/j.zemedi.2018.11.002> (2019).
- Manohar, A. et al. Synthesis and characterization of CeO₂/MgFe₂O₄ nanocomposites for electrochemical study and their cytotoxicity in normal human dermal fibroblast (HDF) and human breast cancer (MDA-MB-231) cell lines. *J. Alloys Compod.* **171932** (2023). <https://doi.org/10.1016/j.jallcom.2023.171932>
- Manohar, A. et al. Zn-doped MnFe₂O₄ nanoparticles for magnetic hyperthermia and their cytotoxicity study in normal and cancer cell lines. *Colloids Surf. A Physicochem. Eng. Asp.* **132037** (2023). <https://doi.org/10.1016/j.colsurfa.2023.132037>
- Manohar, A. et al. Tailored Zn_{1-x}Mg_{0.5}Cu_xFe₂O₄ nanoparticles: Optimizing magnetic hyperthermia for enhanced efficacy and investigating cytotoxicity in normal and cancer cell lines. *Mater. Chem. Phys.* **129050** (2024). <https://doi.org/10.1016/j.matchemphys.2024.129050>
- Manohar, A. et al. Exploring NiFe₂O₄ nanoparticles: Electrochemical analysis and evaluation of cytotoxic effects on normal human dermal fibroblasts (HDF) and mouse melanoma (B16-F10) cell lines. *Colloids Surf. A Physicochem. Eng. Asp.* **132855** (2024). <https://doi.org/10.1016/j.colsurfa.2023.132855>
- Li, X. et al. Metal ions-doped carbon dots: Synthesis, properties, and applications. *Chem. Eng. J.* **430**, 133101. <https://doi.org/10.1016/J.CEJ.2021.133101> (2022).
- Marasini, R., Thanh Nguyen, T. D., Aryal, S. Integration of gadolinium in nanostructure for contrast enhanced-magnetic resonance imaging. *Wiley Interdiscip. Rev. Nanomed. Nanobiotechnol.* **12**. <https://doi.org/10.1002/wnan.1580> (2020).
- Liao, H. et al. One-pot synthesis of gadolinium(III) doped carbon dots for fluorescence/magnetic resonance bimodal imaging. *RSC Adv.* **5**, 66575–66581. <https://doi.org/10.1039/c5ra09948j> (2015).
- Bourlinos, A. B. et al. Gd(III)-doped carbon dots as a dual fluorescent-MRI probe. *J. Mater. Chem.* **22**, 23327–23330. <https://doi.org/10.1039/c2jm35592b> (2012).
- Li, Y. et al. Safe and efficient magnetic resonance imaging of acute myocardial infarction with gadolinium-doped carbon dots. *Nanomedicine* **15**, 2385–2398. <https://doi.org/10.2217/nmm-2020-0160> (2020).
- Zeng, Y. et al. Engineered gadolinium-based nanomaterials as cancer imaging agents. *Appl. Mater. Today* **20**, 100686. <https://doi.org/10.1016/j.apmt.2020.100686> (2020).
- Kuznietsova, H. et al. A comparative multi-level toxicity assessment of carbon-based Gd-free dots and Gd-doped nanohybrids from coffee waste: hematology, biochemistry, histopathology and neurobiology study. *Sci. Rep.* **13**(13), 1–14. <https://doi.org/10.1038/s41598-023-36496-4> (2023).
- Kuznietsova, H. et al. In vitro and in vivo toxicity of carbon dots with different chemical compositions. *Discov. Nano* **18**, 1–17. <https://doi.org/10.1186/s11671-023-03891-9> (2023).
- He, C., Xu, P., Zhang, X. & Long, W. The synthetic strategies, photoluminescence mechanisms and promising applications of carbon dots: Current state and future perspective. *Carbon N Y* **186**, 91–127. <https://doi.org/10.1016/J.CARBON.2021.10.002> (2022).

22. Ai, L. et al. Insights into photoluminescence mechanisms of carbon dots: advances and perspectives. *Sci. Bull.* **66**, 839–856. <https://doi.org/10.1016/j.scib.2020.12.015> (2021).
23. Liu, Z. et al. Size effect of graphene quantum dots on photoluminescence. *Molecules* **26**, 3922. <https://doi.org/10.3390/molecules26133922> (2021).
24. Sadeghi, H. & Dorrani, D. Influence of size and morphology on the optical properties of carbon nanostructures. *J. Theor. Appl. Phys.* **10**, 7–13. <https://doi.org/10.1007/s40094-015-0194-4> (2016).
25. Zhi, B. et al. Synthesis, applications and potential photoluminescence mechanism of spectrally tunable carbon dots. *Nanoscale* **11**, 20411–20428. <https://doi.org/10.1039/C9NR05028K> (2019).
26. Kaur, M. & Bharj, J. Influence of particle size of flame-synthesized carbon nanoparticles on band gap and photoluminescence properties. *Luminescence* **37**, 2123–2128. <https://doi.org/10.1002/bio.4402> (2022).
27. Li, H. et al. Water-soluble fluorescent carbon quantum dots and photocatalyst design. *Angew. Chemie Int. Ed.* **49**, 4430–4434. <https://doi.org/10.1002/anie.200906154> (2010).
28. Zhi, B. et al. Multicolor polymeric carbon dots: synthesis, separation and polyamide-supported molecular fluorescence. *Chem. Sci.* **12**, 2441–2455. <https://doi.org/10.1039/d0sc05743f> (2021).
29. Wang, S. et al. Amino-functionalized graphene quantum dots as cathode interlayer for efficient organic solar cells: Quantum dot size on interfacial modification ability and photovoltaic performance. *Adv. Mater. Interfaces* **6**, 1801480. <https://doi.org/10.1002/admi.201801480> (2019).
30. Zhu, S. et al. The photoluminescence mechanism in carbon dots (graphene quantum dots, carbon nanodots, and polymer dots): Current state and future perspective. *Nano Res.* **8**, 355–381. <https://doi.org/10.1007/S12274-014-0644-3> (2015).
31. Du, X. et al. Size-dependent antibacterial of carbon dots by selective absorption and differential oxidative stress of bacteria. *J. Colloid Interface Sci.* **634**, 44–53. <https://doi.org/10.1016/j.jcis.2022.12.025> (2023).
32. Wang, X. et al. High-yield production of highly fluorinated graphene by direct heating fluorination of graphene-oxide. *ACS Appl. Mater. Interfaces* **5**, 8294–8299. <https://doi.org/10.1021/am402958p> (2013).
33. Palafox, M. et al. Scaling factors for the prediction of vibrational spectra. I. Benzene molecule. *Quant. Chem.* **77**, 661–684. [https://doi.org/10.1002/\(SICI\)1097-461X\(2000\)77:3%3C661::AID-QUA7%3E3.0.CO;2-J](https://doi.org/10.1002/(SICI)1097-461X(2000)77:3%3C661::AID-QUA7%3E3.0.CO;2-J) (2000).
34. Larkin, P. J. *Infrared and Raman Spectroscopy Principles and Spectral Interpretation* 61–62 (Elsevier, 2011).
35. Rap, D. B., Marimuthu, A. N., Redlich, B. & Brünken, S. Stable isomeric structures of the pyridine cation (C₅H₅N⁺) and protonated pyridine (C₅H₅NH⁺) elucidated by cold ion infrared spectroscopy. *J. Mol. Spectrosc.* **373**, 111357. <https://doi.org/10.1016/j.jms.2020.111357> (2020).
36. Coblenz Soc C, Inc. Evaluated infrared reference spectra. in Linstrom, P. J., Mallard, W. G. (eds) *NIST Chemistry Webbook, NIST Standard Reference Database Number 69* (National Institute of Standards and Technology, 2018).
37. Nebogatikova, N. A. et al. Fluorinated graphene dielectric films obtained from functionalized graphene suspension: preparation and properties. *Phys. Chem. Chem. Phys.* **17**, 13257–13266. <https://doi.org/10.1039/C4CP04646C> (2015).
38. Wang, X. et al. High-yield production of highly fluorinated graphene by direct heating fluorination of graphene-oxide. *ACS Appl. Mater. Interfaces* **5**, 8294–8299. <https://doi.org/10.1021/am402958p> (2015).
39. Karlick, F., Kumara, K., Datta, R., Otyepka, M. & Zboril, R. Halogenated graphenes: Rapidly grown family of graphene derivatives. *ACS Nano* **7**(7), 64343–64364. <https://doi.org/10.1021/nn4024027> (2013).
40. Singh, N. P. & Yadav, R. A. Vibrational studies of trifluoromethyl benzene derivatives 1: 2-amino, 5-chloro and 2-amino, 5-bromo benzotrifluorides. *Indian J. Phys.* **75B**, 347–355 (2001).
41. Bloembergen, N. & Morgan, L. O. Proton relaxation times in paramagnetic solutions: Effects of electron spin relaxation. *J. Chem. Phys.* **34**, 337–346. https://doi.org/10.1142/9789812795809_0015 (1996).
42. Sudolská, M. et al. Nature of absorption bands in oxygen-functionalized graphitic carbon dots. *J. Phys. Chem. C* **119**, 13369–13373. <https://doi.org/10.1021/acs.jpcc.5b04080> (2015).
43. Jiao, M. et al. Gadolinium doped red-emissive carbon dots as targeted theranostic agents for fluorescence and MR imaging guided cancer phototherapy. *Chem. Eng. J.* **440**, 135965. <https://doi.org/10.1016/J.CEJ.2022.135965> (2022).
44. Zaderko, A. WO/2020/121119 The process for obtaining of fluoralkylated carbon quantum dots. In *World Intellect. Prop. Organ* (2020). <https://patentscope.wipo.int/search/en/detail.jsf?docId=WO2020121119>
45. Berger, E. et al. Pathways commonly dysregulated in mouse and human obese adipose tissue: FAT/CD36 modulates differentiation and lipogenesis. *Adipocyte* **4**, 161–180. <https://doi.org/10.4161/21623945.2014.987578> (2015).

Author contributions

NZ: Validation, Formal analysis, Investigation, Writing – original draft; KP: Validation, Investigation; AT: Validation, Investigation; AZ: Synthesis, Validation, Investigation, Formal analysis; AG: Validation, Investigation, Formal analysis; TB: Formal analysis, Writing – review & editing; LG: Synthesis, Investigation; RM: Formal analysis, Writing – review & editing; VS: Formal analysis, Writing – review & editing; GM: Conceptualization, Validation, Formal analysis, Supervision, Writing – original draft; VL: Conceptualization, Validation, Supervision, Funding acquisition, Project administration, Writing – review & editing.

Funding

This research work was funded by EU Horizon 2020 Research and Innovation Staff Ex-change Programme (RISE) under Marie Skłodowska-Curie Action (project “UNAT” №101008159). A.N. Zaderko is grateful to French Government for financial support in frame of PAUSE program.

Declarations

Competing interests

The authors declare no competing interests.

Additional information

Supplementary Information The online version contains supplementary material available at <https://doi.org/10.1038/s41598-024-76500-z>.

Correspondence and requests for materials should be addressed to V.S.

Reprints and permissions information is available at www.nature.com/reprints.

Publisher's note Springer Nature remains neutral with regard to jurisdictional claims in published maps and institutional affiliations.

Open Access This article is licensed under a Creative Commons Attribution-NonCommercial-NoDerivatives 4.0 International License, which permits any non-commercial use, sharing, distribution and reproduction in any medium or format, as long as you give appropriate credit to the original author(s) and the source, provide a link to the Creative Commons licence, and indicate if you modified the licensed material. You do not have permission under this licence to share adapted material derived from this article or parts of it. The images or other third party material in this article are included in the article's Creative Commons licence, unless indicated otherwise in a credit line to the material. If material is not included in the article's Creative Commons licence and your intended use is not permitted by statutory regulation or exceeds the permitted use, you will need to obtain permission directly from the copyright holder. To view a copy of this licence, visit <http://creativecommons.org/licenses/by-nc-nd/4.0/>.

© The Author(s) 2024